Journal of Building Engineering 44 (2021) 103223

Contents lists available at ScienceDirect

Journal of Building Engineering

journal homepage: www.elsevier.com/locate/jobe

Multi-objective optimisation of a graphite-slag conductive composite applying a BAS-SVR based model

Junbo Sun [a,b], Xiangyu Wang [c,*], Junfei Zhang [d], Fan Xiao [e], Yuantian Sun [f], Zhenhua Ren [g], Genbao Zhang [h], Shukui Liu [f], Yufei Wang [c,**]

[a] Chongqing University Lndustrial Technology Research Lnstitute, Chongqing University, Chongqing, 400045, China
[b] Institute for Smart City of Chongqing University in Liyang, Chongqing University, Jiangsu, 213300, China
[c] School of Design and Built Environment, Curtin University, Perth, WA, 6102, Australia
[d] School of Civil and Transportation Engineering, Hebei University of Technology, 5340 Xiping Road, Beichen District, Tianjin, 300401, China
[e] College of Management, Zhongkai University of Agriculture and Engineering, Guangzhou, 510225, China
[f] State Key Laboratory for Geomechanics and Deep Underground Engineering, China University of Mining and Technology, Xuzhou, 221116, China
[g] School of Building Engineering, Hunan Institute of Engineering, Hunan, 411228, China
[h] College of Civil Engineering, Hunan City University, Yiyang, Hunan, 413000, China

ARTICLE INFO

Keywords:
Multi-objective optimisation
Graphite
Waste slag
Mechanical strength
Electrical resistivity

ABSTRACT

Electrically conductive cementitious composites (ECCC) possesses numerous virtues including low resistivity and high strain sensitivity, which can be applied as a conductive sensor to monitor structural health. This study produced ECCC with three conductive ingredients, consisting of graphite powder (GP), ground granulated blast-furnace slag (GGBS), and steel slag (SS). The uniaxial compressive strength (UCS), flexural strength (FS), and electrical conductivity were investigated, which showed that the GP enhanced the conductivity more remarkably than the other conductive materials. However, it simultaneously reduced the UCS and FS of ECCC. Also, ECCC samples containing SS had higher FS and conductivity than that containing GGBS. To overcome the challenge of excessive variables, this study introduced an artificial-intelligence (AI) based multi-objective optimisation (MOO) model with 252 samples for the FS test and 336 samples for the resistivity experiment. The support vector regression (SVR) was trained with hyperparameters tuned by the beetle antennae search (BAS). The high correlation coefficients (0.981) were achieved on both test sets. The BAS-SVR model acted as the objective function to develop the multi-objective beetle antennae search algorithm (MOBAS-SVR). The Pareto front of a tri-objective mixture optimisation design for ECCC (cost, FS, and resistivity) was successfully obtained as a design reference. Furthermore, sensitivity research was implemented to comprehend the importance of the variables for the FS and electrical resistivity.

1. Introduction

Cementitious composite is widely used in the construction industry since it yields convenient usage, low cost, reliable durability, and excellent mechanical properties [1,2]. However, excessive cracking elongation may result in brittle failure and the damaging information is hard to directly acquire from external structure [3,4]. Thereby, the internal health monitoring system is the key to prevent sudden failure. The electrically conductive cementitious composite (ECCC) has superior electrical conductivity and can be used as a detection sensor to detect the internal electrical resistance, providing real-time information of structure [5,6]. Compared to the traditional structural materials, self-sensing concrete has the benefit of high sensitivity, acceptable mechanical performance, and natural compatibility without additional sensors for monitoring [1,7]. The self-sensing ECCC has been applied to practice in versatile forms (e.g. bulk, coating, sandwich, bonded, and embedded forms) [7]. Therefore, ECCC can be considered as a reliable and promising self-sensing material that is in great demand in practical application [1].

To improve the electrical ability, conductive ingredients are added to ECCC [7,8]. Graphite powder (GP) is attractive due to its lightweight and high conductivity. Nevertheless, GP equips a smooth surface in the

* Corresponding author. Curtin University, Perth, WA, 6102, Australia.
** Corresponding author.
E-mail address: Xiangyu.Wang@curtin.edu.au (X. Wang).

https://doi.org/10.1016/j.jobe.2021.103223
Received 15 April 2021; Received in revised form 17 August 2021; Accepted 30 August 2021
Available online 5 September 2021
2352-7102/© 2021 Elsevier Ltd. All rights reserved.

microstructural scale, which lessens the surface bonding strength and consequently reduces the mechanical properties [9]. Thereby, the conductivity and the strength of ECCC need to be balanced. To this end, metal waste slags are also introduced to ECCC, including steel slags (SS) and granulated blast-furnace slag (GGBS), which are generated from the steel fabrication and iron slag quenching, respectively. Both SS and GGBS are characterised by crystallization and roughness, which effectively cohere aggregates and intensify the endurance and mechanical strength of the concrete [10,11]. The GGBS possesses high hydraulic reactivity and certain conductivity, contributing to the cement hydration and simultaneously maintaining relatively high conductivity [12,13]. Moreover, GGBS improves the resistance of sulfates, chlorides, alkali-silica reaction, and thermal cracking [14–16]. SS contains numerous iron oxides (*FeO*, Fe_2O_3, and Fe_3O_4) and other metal oxides. Although Fe_2O_3 has low conductivity, *FeO* and Fe_3O_4 have low electrical resistivity of 5×10^{-2} and 4×10^{-3} Ω·cm, respectively (basically the same as that of pitch-based carbon fiber) [17]. Therefore, the electrical conductivity of SS is at the level typical for semiconductors. And the varying square sharp edges around the surface of SS can form a conductive network with GP [18]. Therefore, the combination of slag ensures outstanding electrical conductivity and adequate mechanical strength.

From the aspect of sustainability, the introduction of SS and GGBS in ECCC improves cost-effectiveness and simultaneously reduces environmental pollution [19,20]. The steel industry produces numerous SS and GGBS annually, but the treatment is expensive and time-consuming [21]. They are usually discarded in landfills, posing a significant hazard to public health, soil, and water. Therefore, seeking a feasible way to cope with this problem is essential. Because SS and GBSS exhibit pozzolanic characteristics, they can be used to replace cement to reduce carbon dioxide emissions [22,23].

Concrete normally has enormous compressive strength and relatively low tensile strength so that most cracking appears in the tensile region other than the compressive region. The flexural strength (FS) is usually used to design concrete pavements, beams, and slabs, estimating the tensile stress that causes cracking and evaluating deflections at service loads. Besides, FS is a vital parameter in the application of structural health monitoring [7]. Thereby, FS is reasonable to be investigated owing to its vital influence in construction design and SHM application. Apart from FS, electrical resistivity is an absolutely crucial criterion for ECCC utilisation [9,24]. To assess the effect of conductive ingredients on mechanical strength and electrical resistivity, specimens containing different amounts of GP, SS, and GGBS were prepared and tested. However, the lab-based approach wastes time and energy because numerous samples and testing equipment are required [25–27]. Besides, the outcome can only be obtained with limited mixtures and the application of reasonable regression function is challenging because it requests adequate experience [28–30]. Hence, to get resistivity and FS with arbitrary mixture proportions, the relationship between FS/resistivity and the influencing variables needs to be quantitatively determined.

To this end, machine learning (ML) models are proposed for anticipating the FS and electrical resistivity of ECCC, such as the artificial neural network (ANN) and support vector regression (SVR) [32]. The SVR model has been broadly utilised in the information mining field because of its great generalization capacity and quick calculation capacity [33,34]. Many specialists have remarked on its good noise resistance, excellent generalisation ability, and quick learning velocity compared to the other ML models [35,36]. The SVR model can cope with classification problems, together with linear or non-linear tasks [37]. Also, it can calculate a linear regression function by mapping to the higher dimensional space while simultaneously decreasing the complexity [38,39]. Therefore, the SVR model is chosen for data prediction. However, the performance of the SVR model is restricted on its hyperparameters which are difficult to adjust utilising conventional optimisation strategies [40,41]. Hence, several optimisation algorithms have been proposed, such as genetic algorithm (GA) [19], firefly algorithm (FA) [42], and particle swarm optimisation (PSO) [43], but they are computationally intensive. The beetle antennae search (BAS) algorithm is another optimisation approach, having much less calculation time [44,45]. Therefore, the BAS algorithm is selected for hyperparameters adjustment of the SVR model.

The BAS-SVR based multi-objective optimisation model (MOBAS-SVR) is then established to optimise the mixture proportions of ECCC utilising a metaheuristic algorithm [46–48]. The single-objective optimisation method is not considered since the concrete design is usually complicated which requires simultaneous consideration of multi targets such as cost, FS, slump, etc. The multi-objective optimisation approach (MOO) can optimise multiple objectives under highly nonlinear constraints by proposing Pareto solutions. For instance, the strength, slump, and cost of the plastic concrete were optimised using a multi-objective PSO algorithm by Zhang et al. [49]. Therefore, the MOBAS-SVR was proposed to optimise the cost, FS, and resistivity of ECCC.

In this study, the experiments of FS and electrical resistivity were conducted to investigate the influence of three conductive materials (GP, SS, and GGBS) of ECCC. In total, 90 and 252 samples were cast for the UCS and FS tests, respectively, together with 336 samples prepared for the resistivity test. The datasets of FS and resistivity of ECCC acquired from the laboratory tests were then used to train the SVR models with hyperparameters tuned by the BAS algorithm. The MOBAS-SVR was then proposed based on a weighted sum method to obtain the Pareto optimal solutions considering three objectives: cost, FS, and resistivity. Finally, A sensitive study was carried out to understand the degree of dependency of the outcome on input variables.

2. Experimental program

2.1. Mixture design

The ordinary Portland cement is OPC, P.O 52.5R, and the silica sand is served as fine aggregate with a fineness modulus of 2.6 and particle diameter ranging from 0.2 mm to 0.4 mm. The coarse aggregate is gravel with particle size ranging between 5 mm and 10 mm. The GP, produced by GRF Ltd, China, is chosen as the primary conductive filler [50]. It has high purity (98.5%) and excellent electrical conductivity. The SS and GGBS are the other two conductive fillers, which were purchased from Yuanheng Co. LTD, China. The physical properties and chemical content of cement, GP, SS, and GGBS are presented in Table 1.

The water to binder (SS, GGBS, and OPC) ratio and aggregate to binder ratio were fixed to 0.35 and 4.86, respectively. The percentage of fine aggregate to coarse aggregate was 0.4 for all mixes. Besides, the GP to binder ratios were 2%, 4%, and 6%, and the GGBS or SS were used to replace the cement by 10 wt%, 15 wt%, and 20%. The UCS and FS tests were implemented on the sample under 7, 14, and 28 curing days, while the electrical resistivity test was tested on 7, 14, 21, and 28 days. The FS and resistivity tests were conducted on all the samples with varying content combinations of GGBS, SS, and GP, whereas the UCS test was implemented on specific samples with the same content of GGBS and SS. Three specimens with the same mixture were analysed, and their average UCS, FS, and resistivity values were recorded and presented in Appendix A.

2.2. Sample preparation

The cement and fine and coarse aggregate were thoroughly mixed in a container for 5 min. The SS and GGBS were then added and mixed for another 30 s to ensure uniform distribution. At the same time, the water was weighed and separated in half. The first half was used to wet the composite and blended for 80 s. Subsequently, the other half was sprayed onto the composite for an additional 200 s. After 30 s of the vibration to avoid the increase in the porosity, the composite material

Table 1
The physical and chemical properties of cement, GP, SS, and GGBS.

Cement		GGBS	
Chemical composition		Chemical composition	
CaO	63.40%	CaO	37.14%
SiO_2	20.10%	SiO_2	31.00%
Al_2O_3	4.60%	Al_2O_3	15.60%
Fe_2O_3	2.80%	MgO	8.51%
SO_3	2.70%	SO_3	2.40%
MgO	1.30%	Fe_2O_3	1.80%
Na_2O	0.60%	MnO	0.10%
Total chloride	0.02%		
Physical Properties		**Physical Properties**	
Specific gravity	3.0–3.2 t/m^3	Specific gravity	2.84 t/m^3
Fineness index	390 m^2/kg	Specific surface area	472 m^2/kg
Normal consistency	27%	Relative strength	100%
Setting time initial	120min	Pozzolanic Activity (7 days)	78%
Setting time final	210min	Ignition loss	0.6%
Loss on ignition	3.80%	Particle size distribution	23–37.4 μm
Graphite Powder Chemical composition		**Steel Slag Chemical composition**	
Carbon	Carbon	CaO	31.49%
Ash Content	Ash Content	SiO_2	14.60%
Al_2O_3	5.71%	Al_2O_3	5.71%
MgO	13.8%	MgO	13.80%
SO_3	2.40%	SO_3	2.40%
Fe_2O_3	21.3%	Fe_2O_3	21.30%
Physical Properties		**Physical Properties**	
Bulk Density	0.33 t/m^3	Specific gravity	3.67 t/m^3
Melting Point	4200°C	Relative strength	100%
Moisture Content	0.35%	Temperature rise	18.8OC
Particle size distribution	10–37.4 μm	Particle size distribution	50–75 μm

was poured into a steel mold (400 × 100 × 100 mm) for resistivity test, a mold (50 × 50 × 50 mm) for UCS test, and a mold (40 × 40 × 160 mm) for FS test. After casting, the samples were immediately transferred to a wet cabinet with appropriate humidity (95 ± 5%) and temperature (20 ± 1 °C) for 24 h. Then, the specimen was demoulded and stored in the wet cabinet to the designated days. Before conducting the electrical test, the specimens were placed in the air for 2 days to diminish the wetting influence on the ECCC electrical conductivity.

2.3. Mechanical test

For each mix, the UCS and FS of ECCC were determined as the average value of three parallel specimens at the 7th, 14th, and 28th days as per Chinese National Testing Standards GB/T 50081–2002 [51]. A servo-hydraulic machine (YAW-4206) was used to obtain the peak UCS with a loading rate of 0.5 MPa/s. The FS of specimens was automatically achieved via a three-point bending machine at a constant loading rate of 0.3 MPa/s. The flexural strength f_t (MPa) was calculated by Equation (1).

$$f_t = \frac{3FL}{2bh^2} \tag{1}$$

where F is the fracture load (N); L, h, and b are the span length, and the height and width of the cross section (mm), respectively.

2.4. Electrical test

Both GGBS and SS possess a low hydration rate, however, the slow slag hydration would not significantly influence the whole mortar hydration degree when the slag content was low [52,53]. The ML models can also provide a prediction for long-term ECCC conductive behaviour. Therefore. The resistivity of ECCC was determined by utilising the four-pole method at 7, 14, 21, and 28 days [54]. The four metal mesh electrodes (100 mm × 100 mm) were inserted into the sample with an in$\rho = \frac{UA}{IL}$terval of 120 mm as shown in Fig. 1a. The final conductivity values were averaged from the three identical samples for each mix by a digital multimeter (Keithley Model 2002) through a copper wire. The ECCC samples are shown in Fig. 1b and the electrical resistivity ρ is calculated according to Equation (2).

$$\rho = \frac{UA}{IL} \tag{2}$$

where U represents voltage; A is the sectional area of the specimen; I and L are the electric current and the distance between electrodes, respectively.

3. Multi-objective optimisation methodology

The optimisation design of ECCC follows the methodology of MOBAS-SVR with the process presented in Fig. 2. This starts from the construction of two SVR models to predict the values of FS and electrical resistivity. The hyperparameters of SVR are tuned by BAS and 10-fold cross-validation (CV). Then, the unit price and density are defined to calculate the cost of each mix. Finally, the FS, resistivity, and cost are set as three optimised objectives by applying a multi-objective function based on the weighted sum method. The Pareto front is produced to show the optimisation mixture design of ECCC.

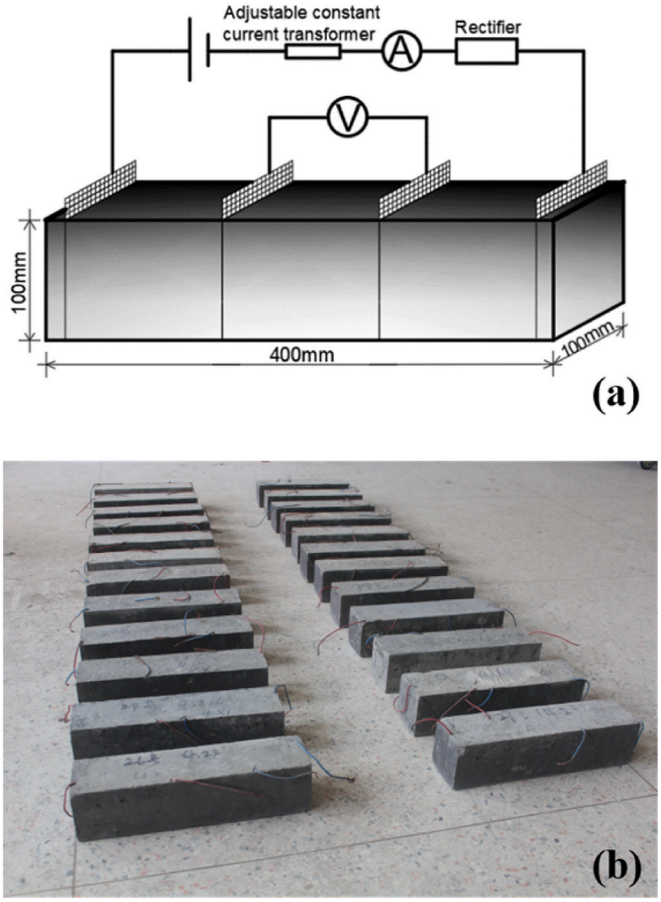

Fig. 1. The diagram of (a) the four-electrode method and (b) ECCC samples.

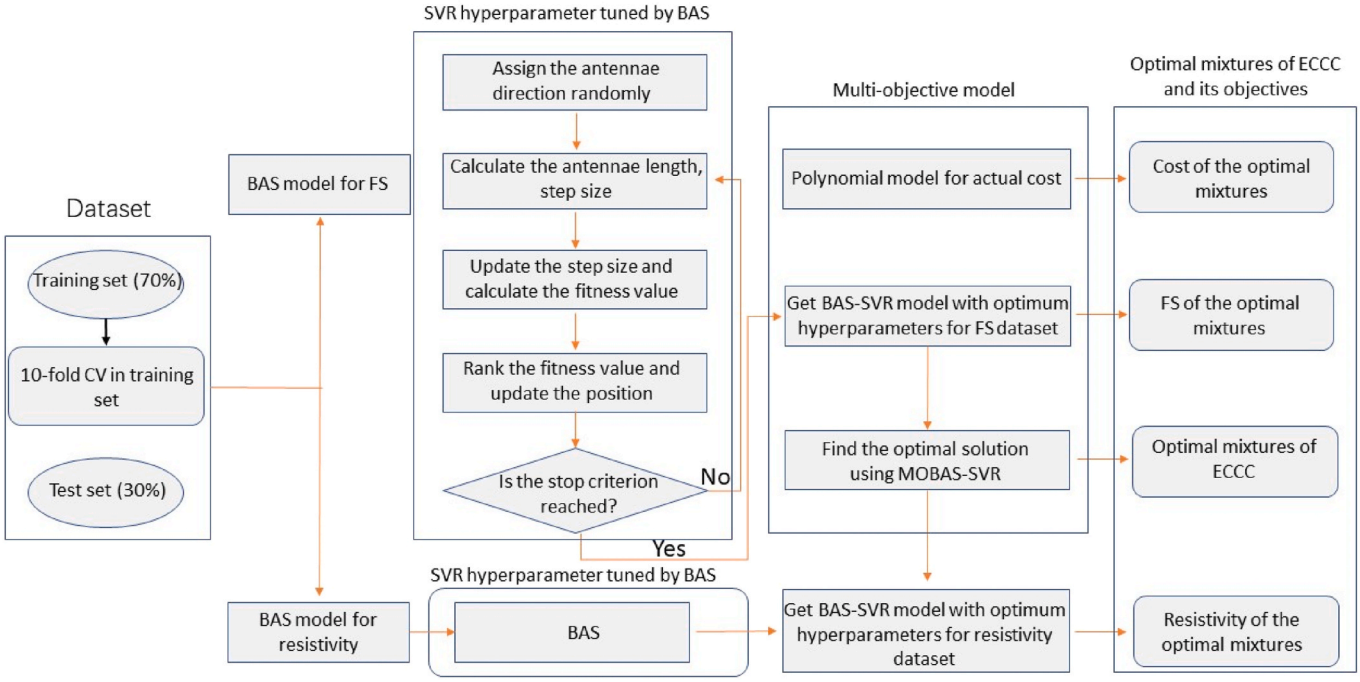

Fig. 2. Flowchart of the MOBAS-SVR system for ECCC optimisation design.

3.1. Data description

The datasets are gathered from the results of 252 samples from the FS test and 336 samples from the conductivity test. The input factors incorporate the age, and the content of cement, GP, SS, and GGBS, and the output variables are FS and electrical resistivity of ECCC. The information of the variables is summarised in Table 2 and Table 3.

The correlation between input variables of FS and Resistivity datasets is demonstrated in Fig. 3. The correlations between different variables are shown less than around 0.5, which proves they are independent without the multicollinearity problems. Thereby, the BAS-SVR model can be successfully established for AI-based multi-objective optimisation design.

3.2. Objective function: BAS-SVR based model

3.2.1. Support vector regression (SVR)

SVR is a frequently used regression method established by Vapnik (1995). It can solve the nonlinear problem by organizing data from the sample space to the higher dimensional space, which is achieved by the Kernel function [55]. The data is described as (x_i, y_i) where x_i is a one-dimensional vector and y_i is the scalar regression value. The training dataset is n groups described in Equation (3) and the regression function is written as Equation (4).

$$\{(x_1, y_1), (x_2, y_2), \ldots, (x_n, y_n)\} \tag{3}$$

$$f(x) = w \cdot \phi(x) + \beta \tag{4}$$

Table 2
Statistics of input and output variables for the FS dataset.

Input Variables	Minimum	Maximum	Mean	Std Dev.
Cement (kg/m^3)	270	450	315	36.41
GP (kg/m^3)	0	27	18	8.10
SS (kg/m^3)	0	90	67.5	22.37
GGBS (kg/m^3)	0	90	67.5	22.37
Age (day)	7	28	22.5	8.75
FS (Mpa)	1.8	4	2.87	0.54

Table 3
Statistics of input and output variables for the Resistivity dataset.

Input Variables	Minimum	Maximum	Mean	Std Dev.
Cement (kg/m^3)	270	450	315	35.92
GP (kg/m^3)	0	27	18	7.99
SS (kg/m^3)	0	90	67.5	22.06
GGBS (kg/m^3)	0	90	67.5	22.06
Age (day)	7	28	17.5	7.86
Resistivity (Ω·cm)	3.93×10^2	4.21×10^6	4.98×10^4	5.41×10^5

where w and β are the weight vector and bias; $\phi(x)$ is a mapping function. The loss function is also introduced as Equation (5) to determine the deviation degree between $f(x_i)$ and y_i.

$$\mathscr{L}(x, y, f) = |y_i - f(x_i)|_e = \begin{cases} 0, & |y_i - f(x_i)| < e \\ |y_i - f(x_i)| - e_i, & |y_i - f(x_i)| \geq e \end{cases} \tag{5}$$

where e illustrates the largest tolerance error, which means that the training points are not penalised if they are within the e-tube. The problem is described as follows with the minimal structural risk considered [56].

$$\mathscr{R}(w) = \frac{1}{2} w^2 + \sum_{i=1}^{n} \mathscr{L}(x, y, f) \tag{6}$$

To enhance the tolerance of biased data, the slack variables δ_i and δ_i^* are utilised to deal with infeasible constraints. Equation (6) can be transformed into the following convex optimisation function:

$$min_{w,e,\delta,\delta^*}\ \mathscr{R}(w) = \frac{1}{2} w^2 + C \sum_{i=1}^{n} (\delta_i + \delta_i^*)$$

$$s.t \begin{cases} y_i - w \cdot \phi(x) - \beta \leq e + \delta_i \\ w \cdot \phi(x) + \beta - y_i \leq e + \delta_i^* \\ \delta_i \geq 0 \\ \delta_i^* \geq 0 \end{cases} \tag{7}$$

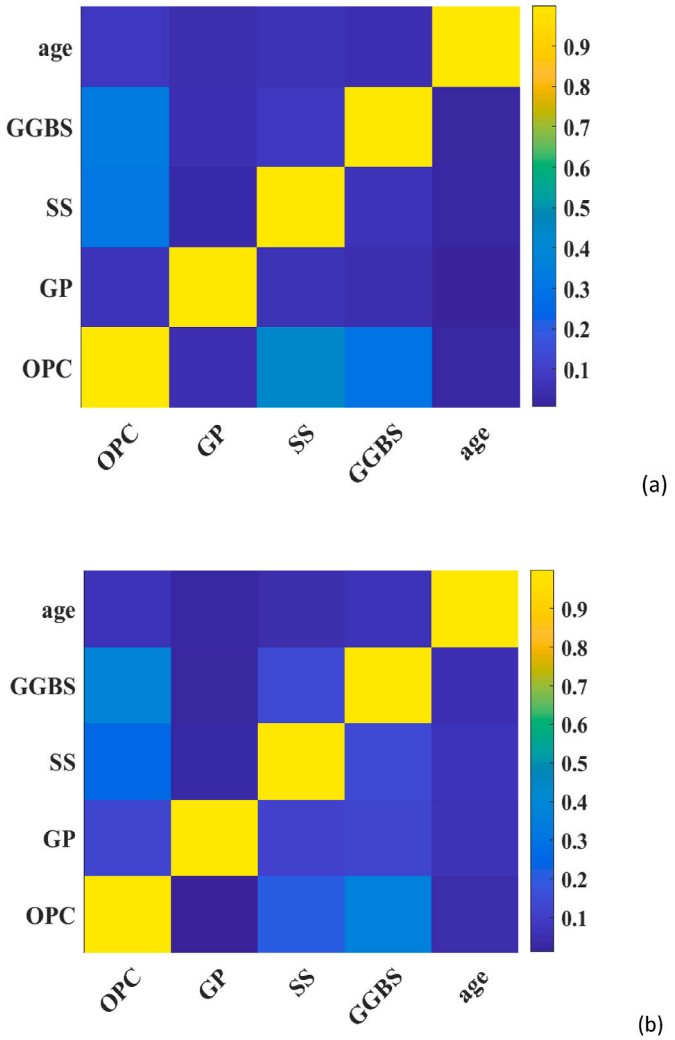

Fig. 3. Correlation matrix of input variables for (a) FS dataset and (b) Resistivity dataset.

where C is the penalty parameter to evaluate the penalising degree of the difference between the regression curve and the samples out of the e-tube.

Fig. 4 presents a schematic diagram of a nonlinear SVR. Subsequently, the prime problem needs to be adjusted to the dual problem by introducing the positive Lagrange multipliers (α_i, α_i^*, u_i, u_i^*) to allow for multiple constraints. The dual function is written as Equation (8).

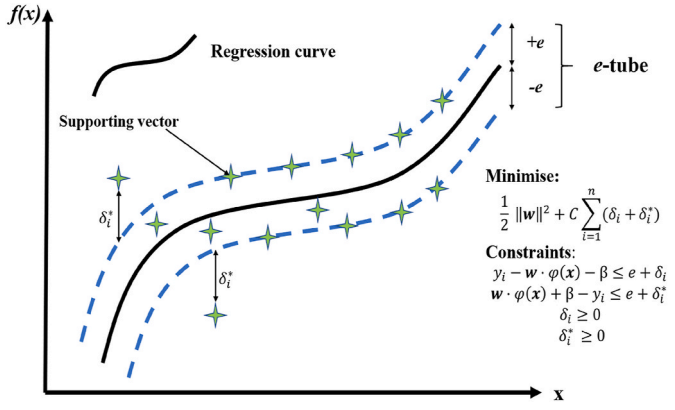

Fig. 4. A support vector regression machine [57].

$$L(w,\beta,\delta,a,u) = \frac{1}{2}w^2 + C\sum_{i=1}^{n}(\delta_i + \delta_i^*)$$
$$-\sum_{i=1}^{n} a_i(e + \delta_i - y_i + w\cdot\phi(x_i) + \beta)$$
$$-\sum_{i=1}^{n} a_i^*(e + \delta_i + y_i - w\cdot\phi(x_i) - \beta)$$
$$-\sum_{i=1}^{n}(u_i\delta_i + u_i^*\delta_i^*) \quad (8)$$

When the constraint equation is seriously opposite to each other, and the objective equation is differentiable, the Karush-Kuhn-Tuck (KKT) rules should be achieved for each of the original and dual points in Equation (9) [58]. According to the KKT, the product of dual variables and constraints in the optimal solution is 0 as shown in Equation (10).

$$\begin{cases} \dfrac{\partial L}{\partial w} = w - \sum_{i=1}^{n}(a_i - a_i^*)\,\phi(x_i) = 0 \\ \dfrac{\partial L}{\partial \beta} = \sum_{i=1}^{n}(a_i - a_i^*) = 0 \\ C - a_i - u_i = 0 \\ C - a_i^* - u_i^* = 0 \end{cases} \quad (9)$$

$$\begin{aligned} &a_i(e + \delta_i - y_i + w\cdot\phi(x_i) + \beta) = 0 \\ &a_i^*(e + \delta_i + y_i - w\cdot\phi(x_i) - \beta) = 0 \\ &(C - a_i)\delta_i = 0 \\ &(C - a_i^*)\delta_i^* = 0 \end{aligned} \quad (10)$$

The Langrage dual problem is finally deduced as follows by solving the above equations.

$$max_i\left(-\frac{1}{2}\sum_{i=1}^{n}\sum_{j=1}^{n}(a_i - a_i^*)(a_j - a_j^*)x_j^T x_j - e \times \sum_{i=1}^{n}(a_i - a_i^*) + \sum_{i=1}^{n} y_i(a_i - a_i^*)\right)$$
$$s.t\begin{cases} \sum_{i=1}^{n}(a_i - a_i^*) = 0 \\ a_i, a_i^* \in [0, C] \end{cases} \quad (11)$$

According to Equation (10), the weight factor w can be obtained as $\sum_{i=1}^{n}(a_i - a_i^*)\phi(x_i)$, and the regression function is given in Equation (12).

$$f(x) = \sum_{i=1}^{n}(a_i - a_i^*)\phi(x_i)x + \beta \quad (12)$$

3.2.2. Beetle antennae search (BAS)

BAS is a metaheuristic algorithm proposed to automatically seek the optimal hyperparameters of the ML models. It is derived from the behaviour of the longhorn beetle [59]. The beetle can perceive the concentration of odour via its two antennae and move towards the orientation where the concentration is dominant. In the BAS algorithm, x_l and x_r indicate the position of left and right antennae, respectively. The superscript i means the i^{th} time instant. Therefore, the position of the antennae at the i^{th} time instant can be defined as Equation (13).

$$x_l^i = x^i + d^i b$$
$$x_r^i = x^i - d^i b \quad (13)$$

where b is a random vector demonstrating the random direction of the beetle. The vector b can be written as Equation (14) by introducing the *rand* and k, illustrating a random function and the dimension, respectively.

$$b = \frac{rand(k,1)}{rand(k,1)} \tag{14}$$

Equation (15) shows the position vector of the beetle where δ means the step size and $f(\mathrm{x})$ represents the fitness function. Besides, the antennae length and the step size can be updated as follows. The pseudocode of BAS is depicted in Fig. 5.

$$x^i = x^{i-1} + \delta^i bsign\left(f\left(x_r^i\right) - f\left(x_l^i\right)\right) \tag{15}$$

$$d^i = 0.95d^{i-1} + 0.01 \tag{16}$$

$$\delta^i = 0.95\delta^{i-1} \tag{17}$$

3.3. Hyperparameter tuning

3.3.1. Cross fold validation

For the SVR model, two basic hyperparameters need to be adjusted, which are Gaussian kernel parameter γ, and namely penalty coefficient c. In order to overcome the overfitting problems, a 10-fold CV is applied. The dataset of FS is randomly split into 30% for the test set and 70% for the training set, as is the resistivity dataset [60]. Afterward, the training set is grouped into 10 commonly exclusive folds presented in Fig. 6 [38]. The nine subsets are used to train the SVR model with hyperparameters tuned by the BAS algorithm after 50 iterations. The remaining one is served as the validation fold to check the reliability of the trained model. The root means square error (RSME) is acquired after the completion of validation. The cross-fold validation is repeated 10 times. Finally, the model having the minimum RSME and optimal hyperparameters will be applied to forecast the resistivity and FS of ECCC in this study.

3.3.2. Performance evaluation

In this study, four accompanying evaluating indicators aim to evaluate the precision of the SVR model: correlation coefficient (R), mean absolute percentage error (MAPE), mean absolute error (MAE), and root mean square error (RMSE). These indicators are calculated as follows [38]:

$$R = \frac{\sum_{i=1}^{n}\left(y_i^* - \overline{y^*}\right)(y_i - \bar{y})}{\sqrt{\sum_{i=1}^{n}\left(y_i^* - \overline{y^*}\right)^2}\sqrt{\sum_{i=1}^{n}(y_i^* - \bar{y})^2}} \tag{18}$$

$$MAPE = \frac{1}{n}\sum_{i=1}^{n}\left|\frac{y_i^* - y_i}{y_i}\right| \tag{19}$$

$$MAE = \frac{1}{n}\sum_{i=1}^{n}\left|y_i^* - y_i\right| \tag{20}$$

$$RSME = \sqrt{\frac{1}{n}\sum_{i=1}^{n}\left(y_i^* - y_i\right)^2} \tag{21}$$

where n is the n groups of data samples; y_i^* and y_i are the predicted and actual results; $\overline{y^*}$ and $\bar{y}$ illustrate the mean values of the predicted and actual results.

3.4. Multi-objective optimisation

3.4.1. Objective function establishment

The BAS-SVR model is adopted as the objective function for resistivity and FS. The third objective function (cost) is computed by polynomials as follows:

$$Cost\left(\$ / m^3\right) = C_c Q_c + C_w Q_w + C_{gp} Q_{gp} + C_{ss} Q_{ss} + C_{ggbs} Q_{ggbs} + C_{fa} Q_{fa} + C_{ca} Q_{ca} \tag{22}$$

In Equation (22), Q_c, Q_w, Q_{gp}, Q_{ss}, Q_{fa}, Q_{ca} and Q_{ggbs} mean the quantity (kg/m^3) of cement, water, GP, SS, GGBS, and fine and coarse aggregate, respectively. Besides, C means the unit price (kg/m^3) of each raw material of ECCC, which is summarised in Table 4.

3.4.2. Constraints

The MOO problem requires setting up the following constraints including range constraints of materials, concrete volume constraints, and ratio constraints.

- Range constraints

Input fitness function $f(x)$, initial step size δ^0 and position of beetle x^0, maximum iterations t, and the ratio of antennae length to step size c
Output optimal position x_b, and optimal fitness function value $f(b)$
For $i = 1$ *to* n
  Generate random antennae direction b
  Calculate the antennae length $d^i = c \times \delta^i$, the positions x_l^i and x_r^i, and the fitness function value $f(x_l^i)$ and $f\left(x_r^i\right)$ at the left and right antennae position
  Calculate the next position x_l^{i+1} and the fitness function value $f(x^{i+1})$
    If $f\left(x^{i+1}\right) < f(b)$
      Update x_b to x^{i+1}
      Update f_b to $f\left(x^{i+1}\right)$
    End
  Update step size δ^{i+1}
End

Fig. 5. The pseudocode for BAS.

Fig. 6. 10-fold cross validation.

Table 4
The unit cost of each variable of ECCC.

Variables	Notation	Unit price ($/kg)	Unit weight (kg/m^3)
OPC	C_c	0.059	3050
Water	C_w	0.0005	1000
GP	C_{gp}	0.71	1800
SS	C_{ss}	0.14	3670
GGBS	C_{ggbs}	0.05	2840
Fine aggregate	C_{fa}	0.009	2600
Coarse aggregate	C_{ca}	0.0065	2700

The data range can be set according to the datasets of FS and resistivity for ECCC, as shown in Equation (23):

$$d_{imin} \le d_i \le d_{imax} \tag{23}$$

where d_{imin} and d_{imax} represent the lowest and highest value of the ith variable.

- Volume constraints

The amount of the solid should amount to one cubic meter as follow:

$$V_m = \frac{Q_c}{U_c} + \frac{Q_w}{U_w} + \frac{Q_{gp}}{U_{gp}} + \frac{Q_{ss}}{U_{ss}} + \frac{Q_{ggbs}}{U_{ggbs}} + \frac{Q_{fa}}{U_{fa}} + \frac{Q_{ca}}{U_{ca}} \tag{24}$$

where U_c, U_w, U_{gp}, U_{ss}, U_{ggbs}, U_{fa} and U_{ca} are the unit weight of OPC, water, GP, SS, GGBS, fine aggregate, and coarse aggregate, individually.

- Ratio constraints

To seek ECCC mixture optimisation, the ratio constraints need to be determined to establish the correlation between different raw materials. Table 5 lists the input factors which depend on the datasets framed.

3.4.3. Construction of MOBAS-SVR

The establishment of MOBAS-SVR is based on the objective functions of FS, resistivity, and cost by applying the weighted sum method. Each objective (f_k) is combined into a single composite objective function (F), shown in Equation (25).

$$F = \sum_{k=1}^{k} w_k f_k \ , \ \sum_{k=1}^{k} w_k = 1 \tag{25}$$

where weights are calculated as $w_k = \frac{p_k}{K}$; k is the uniform distribution number and p_k (ranging from 0 to 1) is the random number developed from a uniform distribution.

Therefore, the above function can be defined as follows in this research:

$$F = w_1 \cdot FS(28\ days) + w_2 \cdot Resitivity(28\ days) + w_3 \cdot cost \tag{26}$$

$$\sum_{k=1}^{3} w_k = 1 \tag{27}$$

Since multiple goals in the MOO problem need to be optimised, the Pareto optimal front is proposed to provide a non-dominated solution, as described as follows [61,62]. It implies the condition that other objective functions fail to be improved without worsening the other functions [61,63]:

If A represents the group of feasible solutions and $x^* \in A$ is one of the Pareto optimal solutions, there is no existence of $x \in A$ satisfy that

$$f_k(x) \le f_k(x^*) for k = 1, 2, 3, \ldots, t and \tag{28}$$

$$f_k(x) < f_k(x^*)\ for at least one k \tag{29}$$

If $f(x^*)$ is larger than $f(x)$ for every x, Pareto optimal solution x^* will be achieved. The combination of Pareto optimal solutions constitutes the Pareto front, which depicts in Fig. 7, representing the collection of non-dominated solutions. The BAS can be developed to MOBAS-SVR through the weight sum method to deal with the Pareto front of MOO problems where the pseudocode is summed up in Fig. 8.

Table 5
The constraints of ECCC input variables.

Variables	Expressions	Lower bound	Upper bound
OPC	C (kg/m^3)	270	360
GP ratio	$C_{gp}/(C_c + C_{ss} + C_{ggbs})$	0.02	0.06
SS ratio	$C_{ss}/(C_c + C_{ss} + C_{ggbs})$	0.1	0.2
GGBS ratio	$C_{ggbs}/(C_c + C_{ss} + C_{ggbs})$	0.1	0.2
SS to GGBS ratio	C_{ss}/C_{ggbs}	0.5	2

3.4.4. Decision-making for multi-objective optimisation designs

The MOO problems can be solved by proposing the Pareto front as demonstrated above, however, the final optimal mixture proportion fails to obtain for decision-making. Thereby, a multi-criteria decision strategy is proposed, which is the technique for order preference by similarity to an ideal solution (TOPSIS). According to the Pareto front which determines the positive and negative ideal points, TOPSIS can select a solution that is closest to the former and meantime farthest from the latter. The ideal point (positive) is the solution in which the value of the composite function is highest and the ideal point (negative) corresponds to the worst object function value. Finally, a solution with the highest C_i is considered as the best one where the formulations depicted as follows:

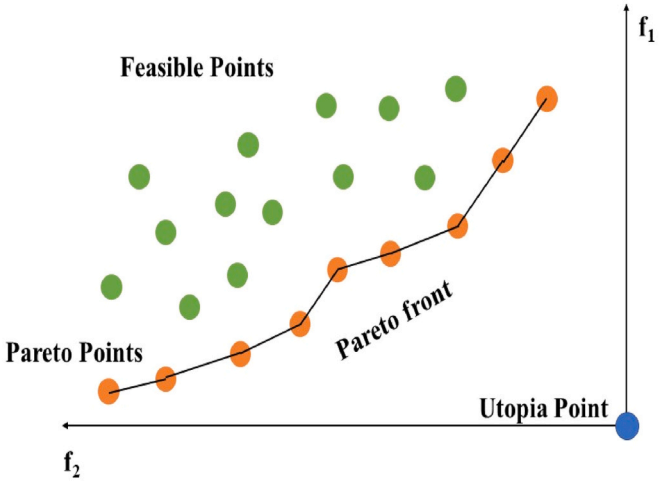

Fig. 7. Model of a Pareto line with feasible points [64].

$$d_{i+} = \sqrt{\sum_{j=1}^{n} \left(F_{ij} - F_j^{ideal}\right)^2} \tag{30}$$

$$d_{i-} = \sqrt{\sum_{j=1}^{n} \left(F_{ij} - F_j^{non-ideal}\right)^2} \tag{31}$$

$$C_i = \frac{d_{i-}}{d_{i+} + d_{i-}} \tag{32}$$

where d_{i+} and d_{i-} are the positive and negative solutions; n and i are the numbers of objectives and the ith Pareto point; F_j^{ideal} represents the ideal value of the jth objective and $F_j^{non-ideal}$ is the non-ideal value.

3.5. Variable importance measure

To explore the relationship between inputs and outputs, a method based on sensitivity analysis (SA) was applied. It can measure the impact on the proposed SVR output when the input value changes within its value range [65,66]. The input and output variables need to be designed at first. Then, each input variable is individually evaluated with all the

Input: fitness function $f_1(x),\ f_2(x), \ldots, f_k(x); x = (x_1, \ldots, x_n)^T$, initial the beetle position $x^0 = (x_1^0, \ldots, x_n^0)$, initial step size $\delta^0 = (\delta_1^0, \ldots, \delta_n^0)$, maximum iterations T, the proportion between antennae length and step size c, and the step size attenuation coefficient α.
Output: M Pareto optimal positions $X_P = (X_{P,1}, \ldots, X_{P,M})$
While $m \le M$
  Set the random weight w_k
  For i= 1 to T
    Generate random antennae direction b^i
    Calculate the antennae length $d^i = c \times \delta_m^i$, the positions x_l^i and x_r^i, and the weighted sum function value $F(x_l^i)$ and $F(x_r^i)$
    Calculate the next position $x^{i+1} = x^i + \delta^i$ and its function value
    If $F(x^{i+1}) < F(b)$
      Update x_b to x^{i+1}, F_b to $F(x^{i+1})$
    End if
    Update step size δ^{i+1}
  End for
  If x_b meet all the constraints
    If x_b is not dominated by X_P
      Update $X_P = X_P \cap x_b,\ m = m + 1$
    End if
    For $X_{P,t}$ in X_P
      If x_b dominates $x_{p,t}$
        Update $X_P = X_P - x_{p,t},\ m = m - 1$
      End if
    End for
  End if
End while

Fig. 8. The pseudocode of MOBAS-SVR.

other variables unchanged. The SA includes global or local analysis, but local sensitivity cannot be used for locating model uncertainties. Global sensitivity analysis (GSA) can assess all input variables to be modified simultaneously. Therefore, GAS was utilised for a ranking of importance among multiple variables in this study. Finally, the modelling of GSA provides the importance of variables through bar charts, ranging from 0 to 100% [67]. The following equations show a gradient metric to estimate the resulting change of the output and the relative importance formulation [67,68].

$$g_\varepsilon = \sum_{j=2}^{L} \frac{\left|\widehat{y_{\varepsilon j}} - \widehat{y_{\varepsilon j-1}}\right|}{L-1} \tag{33}$$

$$R_\varepsilon = g_\varepsilon \Big/ \sum_{i=1}^{I} g_i \tag{34}$$

where ε is the input variable that needs to be analysed; $\widehat{y_{\varepsilon j}}$ stands for the sensitivity response indicator for $x_{\varepsilon j}$; R_ε is the relative importance of the variable.

4. Results and discussion

4.1. Results of laboratory tests

4.1.1. Results of mechanical strength test

Figs. 9 and 10 present the effect of the content of GP, GGBS, and SS on the UCS and FS of ECCC, respectively, when the curing day is 28. The GP adversely influenced the mechanical strength that both UCS and FS decreased with the increase of the GP ratio. This is because the surface of the GP is relatively smooth, which reduces the binding fraction of the interface transition zone (ITZ) of the aggregates [69–71]. When the GGBS and SS were both 20%, the UCS of ECCC containing GP increased from 2% to 4% and 6% decreased by 20.65% and 32.34%, respectively. Similarly, the FS of ECCC decreased by 8.57% and 22.86%, respectively in this case. Besides, both the UCS and FS significantly diminished when the GP ratio increased from 4% to 6% especially when the contents of GGBS and SS were low, indicating a 4% GP ratio as the threshold.

According to the UCS test results, the increasing contents of GGBS and SS generally adversely influenced the mechanical strength of ECCC. Similarly, the FS decreased with the increase of the content of SS and GGBS. The possible reason is that excessive slag can destroy the uniform molecule size distribution in the ECCC, and the insufficient binder fails to fill the gap between aggregates. As a result, the binding fraction scale

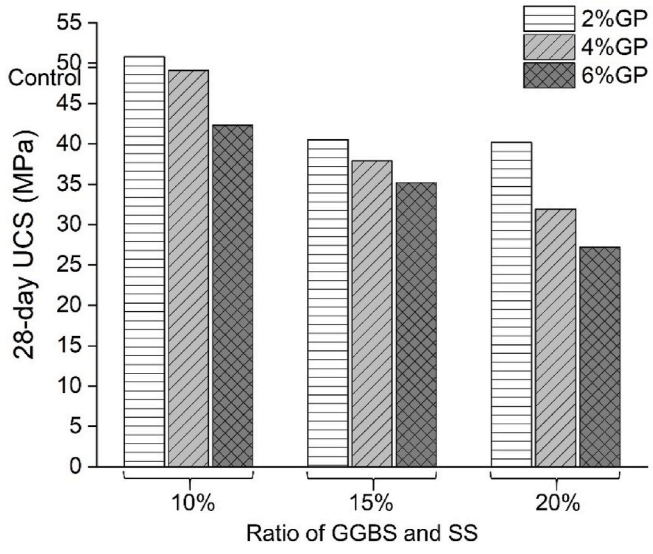

Fig. 9. The UCS of ECCC composites at 28 curing days.

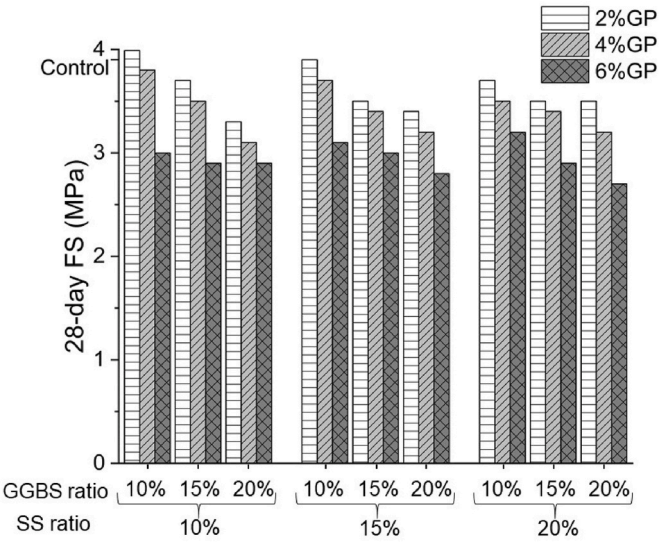

Fig. 10. The FS of ECCC composites at 28 curing days.

decreases, and so does the mechanical strength [72–74]. However, the effect of slags on both UCS and FS was positive on condition their contents were not excessive. Compared with the control sample (UCS = 49.5 MPa, FS = 3.9 MPa), the specimen containing 2% GP, 10% GGBS, and 10% SS possessed higher UCS and FS strength of 4 MPa and 50.8 MPa, which were increased by 2.63% and 2.56%, respectively. This UCS and FS are supposed to be higher than those of the sample with a single 2% GP, indicating the positive influence of GGBS and SS on ECCC's mechanical strength. This can be attributed to the crystal structure of the waste slag, enhancing the interfacial strength of ITZ and improving the microstructural friction. In addition, SS had a less negative effect than GGBS from the FS test results. For example, when the GP was 4%, the FS of ECCC containing 10% SS and 20% GGBS was 3.1 MPa at 28 days, which was lower than the sample containing 15% SS and 15% GGBS (3.4 MPa), and lower than the sample containing 10% GGBS and 20% SS (3.5 MPa). The is because the SS surface has massive angular square crystals approximately 500 nm to 1 μm, which can fundamentally expand the binding strength of ITZ and improve the mechanical properties [75,76].

4.1.2. Results of electrical test

The 14-day and 28-day electrical resistivity of ECCC containing different content of slag solids and GP are depicted in Fig. 11. Compared to the control sample of which the resistivity showed 2.32×10^6 Ω·cm for 14 days and 4.21×10^6 Ω·cm for 28 days, the ECCC composites demonstrated superior conductivity with much lower resistivity values. The conductivity of ECCC was very sensitive to GP that the resistivity experienced a significant downward trend with the increase of GP content. For instance, when the GP proportion increased from 2% to 6%, the electrical resistivity of ECCC containing 10% SS and 10% GGBS at 14 and 28 curing days decreased by 90.85% and 86.53%, respectively. Furthermore, no crucial change in electrical resistivity with different SS and GGBS amounts under the situation of 2% GP addition. Generally, the resistivity decreased with the increase of both SS and GGBS ratio, but SS was more influential than GGBS. For the sample having 4% GP and 20% GGBS, the 28-day electrical resistivity of ECCC was reduced by 47.39% from 9.60×10^3 Ω·cm to 5.05×10^3 Ω·cm when GGBS increased from 10% to 20%. And for the sample containing 4% GP and 20% SS, when the ratio of SS changed from 10% to 20%, the resistivity was reduced by 89.90% from 5.00×10^4Ω·cm to 5.05×10^3 Ω·cm. As a result, SS remarkably enhanced the electrical conductivity and simultaneously compensated the strength loss due to the GP lubrication. Besides, the electrical conductivity of early-age ECCC samples was lower than that of

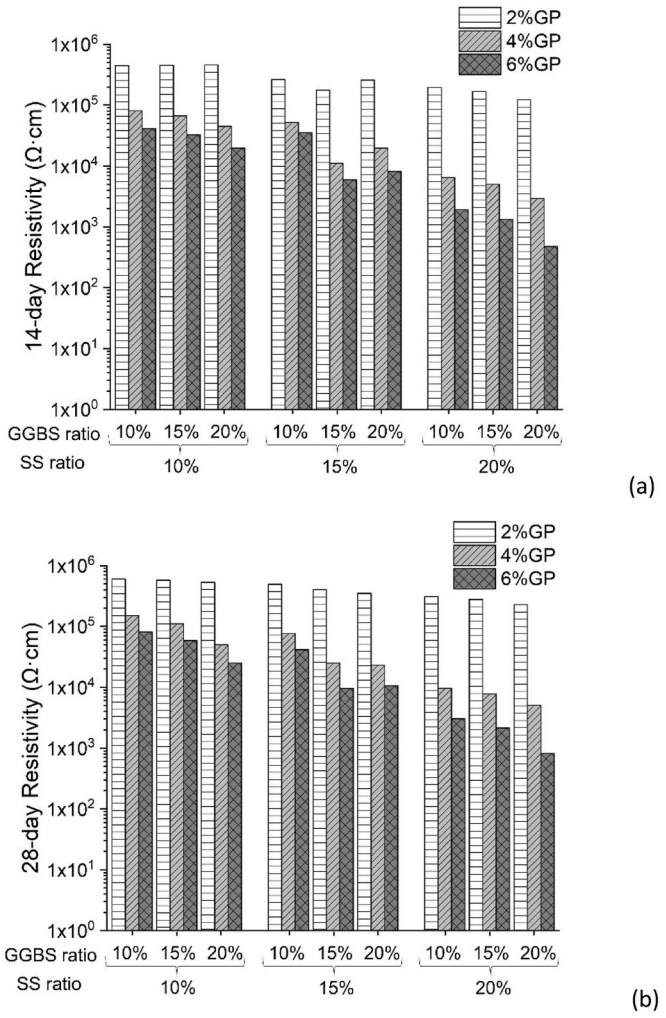

Fig. 11. The electrical resistivity of ECCC composites at (a) 14 days and (b) 28 days.

fully cured concrete, illustrating that the water particles positively affect the conductivity of ECCC. In conclusion, the mechanical and conductive behaviours of SS and GGBS have been exhibited, although samples containing GP without SS and GGBS were not prepared. To predict the reliable properties of ECCC, the machine learning method can be used as demonstrated in the next section.

4.2. Modelling results

4.2.1. Results of hyperparameter tuning

As mentioned above, the hyperparameters (γ and c) need to be adjusted by utilising a 10-fold CV and BAS algorithm. The fold corresponding to the minimum RMSE is shown in Fig. 12. The 4th and 2^{sec} fold showed the minimum RSME in the FS dataset and resistivity dataset, respectively. Fig. 13 depicts the iteration situation on the 4th fold of the FS dataset and the 2^{sec} fold for the resistivity dataset. The RMSE curve needed 9 iterations to converge to 0.028 MPa for the FS set, and 12 iterations to reach 1.25×10^4 Ω·cm for the resistivity set, illustrating the efficiency of tuning the hyperparameters by BAS. Ultimately, the hyperparameters c and γ arrived at 0.11 and 187.8 for FS, and 2.63 and 1152423 for resistivity set, respectively.

4.2.2. Performance of BAS-SVR

Fig. 14 shows the prediction situation of FS and resistivity by employing the optimal SVR model. Most of the points are found to be

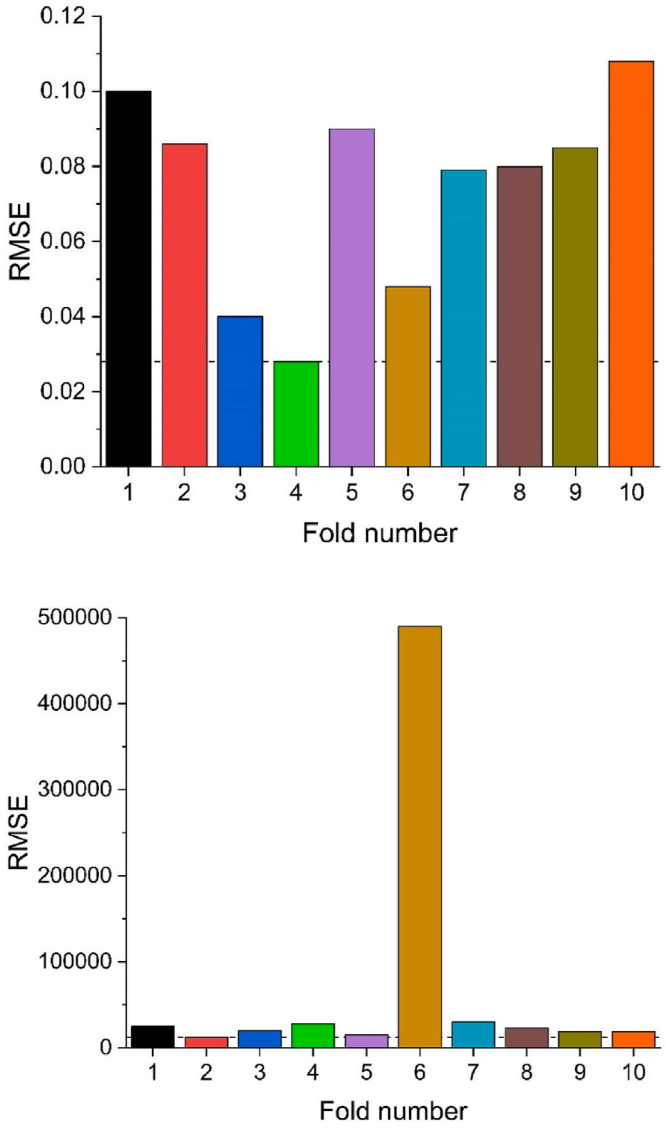

Fig. 12. 10-fold CV in tuning hyperparameters on the (a) FS dataset and (b) resistivity dataset.

close to the perfect fitting curve (the black solid diagonal line), indicating the robustness of the model prediction. The correlation coefficients were up to 0.9906 and 0.9812 in the training and test sets respectively for the FS dataset, showing the high predictive ability of the BAS-SVR model. Similarly, the high R value (0.9806) appeared on the resistivity dataset, although one outlier existed. This illustrated the sufficient accuracy of BAS-SVR models in predicting the values of both FS and resistivity of ECCC. Table 6 lists the values of the evaluation index consisting of R, MAE, MAPE, and RMSE in FS and resistivity aspects. The values of MAE, MAPE, and RMSE were low, further support the low error of BAS-SVR models. In addition, the values of RMSE or R on the training set and test set were both close, which means that the overfitting issue did not happen. Therefore, the model is feasible to predict the properties of ECCC.

4.2.3. ECCC mixture optimisation

Solutions that minimised the objective function were ultimately acquired by using MOBAS-SVR. The cost and 28-day electrical resistivity were minimised simultaneously, while the 28-day FS of ECCC was maximised. As presented in Fig. 15, the Pareto front of the tri-objective (FS, resistivity, and cost) optimisation design has been generated. The

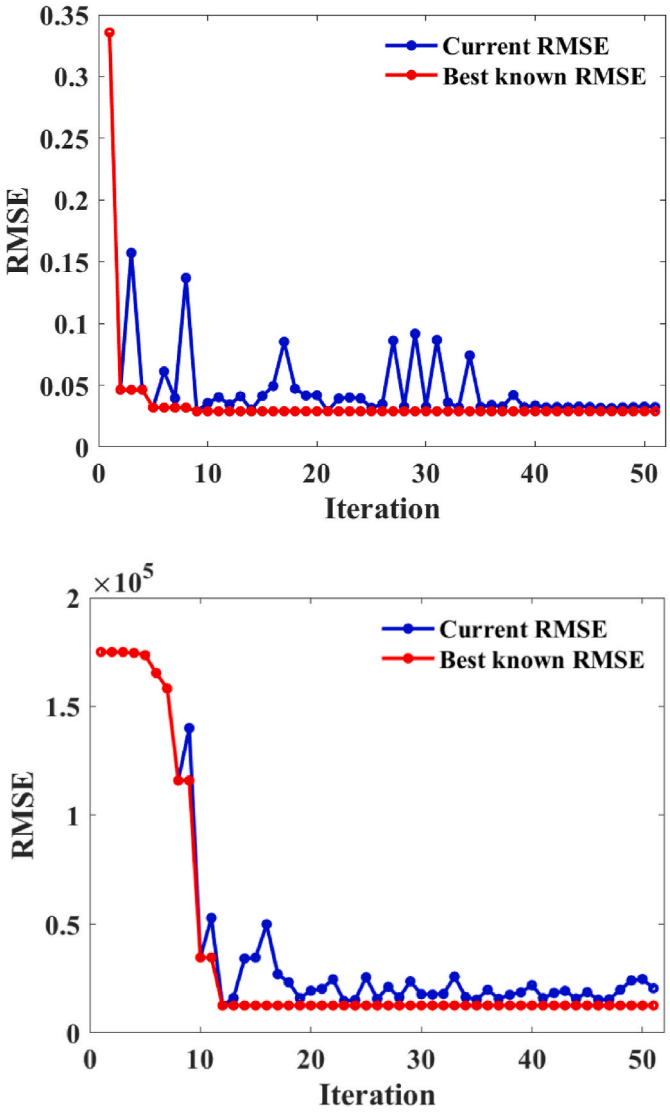

Fig. 13. Normalised RMSE versus iteration in the optimal fold for (a) FS dataset and (b) resistivity dataset.

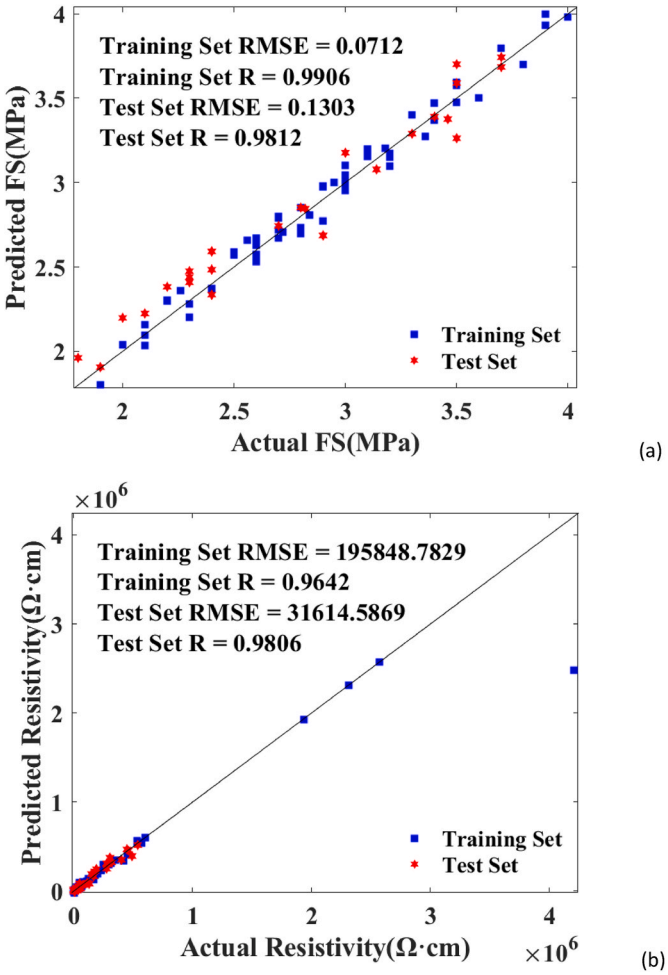

Fig. 14. Actual versus predicted values for (a) FS and (b) resistivity.

Table 6
Evaluation of BAS-SVR on FS and resistivity test sets.

Test category	Evaluation index			
	RMSE	R	MAE	MAPE
FS	0.130 MPa	0.981	0.017 MPa	0.042
Resistivity	3.16×10^4 Ω·cm	0.981	2.32×10^4 Ω·cm	2.476

Pareto front was composed of 100 non-dominated points based on the database and constraints. These points were widely distributed in the three-dimensional space with reasonable ranges of FS, resistivity, and cost. It illustrates the effectiveness and the performance of the generalisation of the MOBAS-SVR model.

To increase the conductivity of ECCC, the cost needs to be increased to lower the resistivity. However, the corresponding FS was inevitable to be reduced. Therefore, the final selection is dependent on the decision-maker to judge the dominant property of ECCC and balance the property and budget. Point A, B, C, and D are four selected Pareto solutions, among which point B, C, and D correspond to the single objective optimisation design. In point B, the FS of the ECCC reached the highest with FS equaled 3.6 MPa. And in points C and D, the minimum electrical resistivity and cost were found respectively, which means the single optimised resistivity and cost of ECCC in the tri-objective optimisation problem have been achieved. Besides, with the application of the TOPSIS method, point A was determined as the most appropriate solution. It has the highest TOPSIS score of 1 with 3.50 MPa FS, 2.69×10^5 Ω·cm resistivity, and 49.98 $/m^3 cost. The corresponding mixture proportions of solutions A, B, C, and D are listed in Table 7. Generally, the decision-maker should balance the budget and the properties of ECCC that need to be attained, otherwise, the ideal solution with the highest TOPSIS is preferable.

4.2.4. *Variable importance of using BAS*

The sensitivity study outcomes present the estimation impacts of measurement variables on FS and resistivity, as illustrated in Fig. 16. The curing time had the most significant influence on the FS dataset with the highest influence ratio of 45.29%. Within the three conductive materials (GP, SS, and GGBS), GP showed the highest importance ratio of 28.37%, followed by GGBS (13.99%). The importance ratio of the SS was negligible and found to be 0.1%. This result is in agreement with the afore-mentioned experimental results, illustrating the accuracy of the BAS-SVR model in evaluating the variable importance.

For the ranking of input variables for electrical resistivity of ECCC, GP possessed the highest significant ratio of 48.15%, followed by SS (21.23%) and OPC (19.76). Besides, it was observed that GGBS had the least influence ratio of 9.42% on the resistivity of ECCC. The outcome is in accordance with the experimental result that GP diminished the resistivity of ECCC more significantly than SS and GGBS. Therefore, GP and SS are more appropriate than GGBS to act as the conductive

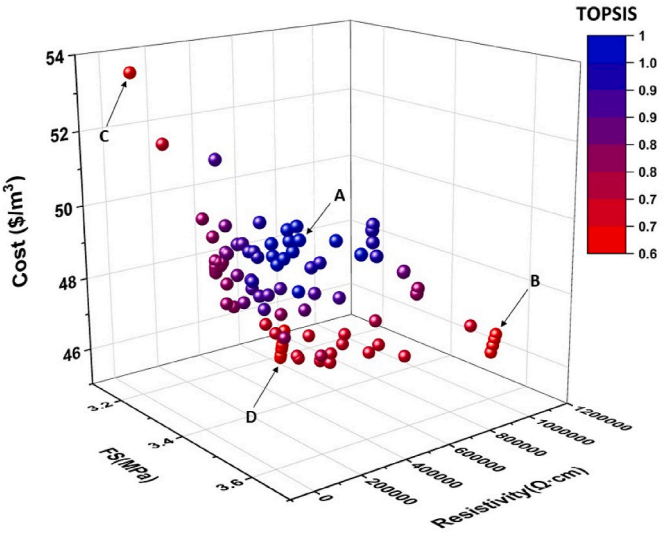

Fig. 15. Pareto front based on cost, FS, and resistivity of ECCC.

Table 7
Mixture proportions of Pareto solutions of ECCC.

Mixture	A (Final point)	B	C	D
OPC (kg/m^3)	305.4	365.0	270	309.4
W (kg/m^3)	157.5	157.5	157.5	157.5
GP (kg/m^3)	9	9	15.73	9
SS (kg/m^3)	90	45	90	45
GGBS (kg/m^3)	60.24	45	90	90
CA (kg/m^3)	1302.6	1302.6	1302.6	1302.6
FA (kg/m^3)	884.6	884.6	884.6	884.6
FS (MPa)	3.50	3.60	3.16	3.34
Resistivity (Ω·cm)	2.69×10^5	1.03×10^6	4.92×10^4	4.30×10^5
Cost ($/m$^{3)}$	49.98	46.77	53.54	45.953
TOPSIS score	1	0.62	0.66	0.67

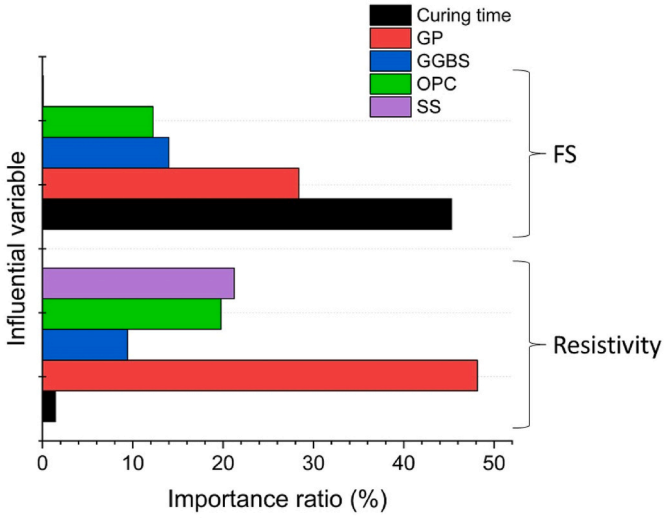

Fig. 16. Input variables importance evaluation for FS and resistivity of ECCC.

materials of ECCC. Furthermore, the importance of curing time on resistivity had a negligible importance ratio of 1.44%, illustrating the less importance of the curing time for electrical conductivity.

5. Conclusion

In this study, UCS, FS, and electrical resistivity tests of ECCC were conducted to investigate the effect of three conductive materials, GP, SS, and GGBS. Based on the experimental datasets, a BAS-SVR based multi-objective optimisation model was proposed to seek the optimal mixture design for cost, FS, and resistivity of ECCC. Besides, the variable importance analysis was carried out and the outcome was consistent with the experimental findings. The following results were drawn from this study:

1. The GP significantly reduced the UCS and FS of ECCC, although the GP content was only 2%, mainly due to the lubrication effect. When the slag solids (SS + BBGS) ratio was low at 20%, the UCS and FS of ECCC slightly increased by 2.63% and 2.56%, respectively, but decreased with the increase of the slag. Additionally, SS had a less negative effect than GGBS on FS.
2. The GP, SS, and GGBS can improve the conductivity of ECCC. The enhancement effect of GP was the highest that the resistivity was decreased by 80%–90% when the GP content was increased from 2% to 6%. Besides, SS had a more significant impact on electrical conductivity than GGBS.
3. The BAS algorithm was competent in adjusting hyperparameters of the SVR model with minimum RMSE obtained at the 4th and 2^{sec} fold on the FS and resistivity dataset, respectively. The R values for both test sets were 0.981, indicating their high accuracy and effectiveness.
4. The MOBAS-SVR successfully generated the Pareto front for tri-objective (cost, FS, and resistivity) problem with nonlinear constraints. It depends on the decision-maker to select the multi-objective optimisation solutions. Otherwise, the design with the highest TOPSIS (point A in Fig. 15) is preferable and more appropriate, with FS equals 3.50 MPa, resistivity equals 2.69×10^5 Ω·cm, and cost equals 49.98 $/m^3.
5. The variable importance ranking shows that the most significant variables were curing time and GP, affecting respectively FS and resistivity, which is consistent with the experimental findings.

In future work, the generalisation property of the MOO model can be improved by collecting a comprehensive information database comprising more conductive materials and long-term mechanical and conductive properties. Furthermore, updated ML should be consolidated and compared to improve the effectiveness, accuracy, and efficiency. The MOO model can be used to design electrically conductive alkali-activated materials with various carbon- or metal-based admixtures. It can also be implemented into practice to improve the design of concrete especially during the early stage of construction.

Author statement

Junbo Sun: conceptualization and methodology. Zhenhua Ren and Genbao Zhang: methodology and formal analysis. Yufei Wang: writing and formal analysis. Junfei Zhang and Shukui Liu: conceptualization, methodology, and revising, Fan Xiao and Yuantian Sun: reviewing and editing. Xiangyu Wang: conceptualization and supervision. All authors contributed to the article and approved the submitted version.

Declaration of competing interest

The authors declare that they have no known competing financial interests or personal relationships that could have appeared to influence the work reported in this paper.

Acknowledgement

The project is supported by National Natural Science Foundation of China (Grant No. 52078181, 52104106, E2019202484), Hunan Key

Laboratory of Intelligent Disaster Prevention and Mitigation and Ecological Restoration in Civil Engineering, Catastrophe and Reinforcement of Dangerous Engineering Structures, Hunan Provincial Engineering Research Center. The project is also funded by Key R&D Project of Hunan Province Intelligent Disaster Prevention and Mitigation and Ecological Restoration in Civil Engineering (2020SK2109).

Appendix A

ID	OPC (g)	GP (g)	SS (g)	GGBS (g	CA (g)	FA (g)	W (g)	FS (MPa)			UCS (MPa)			Resistivity (Ω·cm)			
								7d	14d	28d	7d	14d	28d	7d	14d	21d	28d
1	450	0	0.0	0.0	1302.6	884.6	157.5	3	3.5	3.9	38.1	44.6	49.5	1933751	2315122	2572178	4205411
2	360	9	45.0	45.0	1302.6	884.6	157.5	3	3.6	4	38.1	45.7	50.8	304972	447514	533701	601659
3	360	18	45.0	45.0	1302.6	884.6	157.5	2.7	3.3	3.8	35	43.5	49.1	76807	81325	159036	151125
4	360	27	45.0	45.0	1302.6	884.6	157.5	2.3	2.8	3	26.5	36	42.3	40000	40941	79058	81032
5	337.5	9	45.0	67.5	1302.6	884.6	157.5	2.7	3.36	3.7				294084.8	452165.6	539022.6	573161.8
6	337.5	18	45.0	67.5	1302.6	884.6	157.5	2.5	3.14	3.5				56726.2	66868.2	115238	110666.2
7	337.5	27	45.0	67.5	1302.6	884.6	157.5	2.1	2.56	2.9				27363.6	32448.6	55495.6	58698.8
8	315	9	45.0	90.0	1302.6	884.6	157.5	2.3	3	3.3				277754	459143	547005	530416
9	315	18	45.0	90.0	1302.6	884.6	157.5	2.2	2.9	3.1				26605	45183	49541	49978
10	315	27	45.0	90.0	1302.6	884.6	157.5	1.8	2.2	2.9				8409	19710	20152	25199
11	337.5	9	67.5	45.0	1302.6	884.6	157.5	2.7	3.46	3.9				200291	263572.4	418918.8	490692.4
12	337.5	18	67.5	45.0	1302.6	884.6	157.5	2.6	3.18	3.7				35512.4	51671.4	64986.2	76730.2
13	337.5	27	67.5	45.0	1302.6	884.6	157.5	2.4	2.84	3.1				21985	35320.4	37412.2	41496.4
14	315	9	67.5	67.5	1302.6	884.6	157.5	2.4	3.1	3.5	28.5	35.5	40.5	121673	177947	250950	401248
15	315	18	67.5	67.5	1302.6	884.6	157.5	2.3	2.95	3.4	26.9	33	37.9	6701	11082	15893	24985
16	315	27	67.5	67.5	1302.6	884.6	157.5	2.1	2.6	3	18.1	25.8	35.2	4963	5948	6277	9559
17	292.5	9	67.5	90.0	1302.6	884.6	157.5	2.2	2.82	3.4				165252.8	257569.4	319318.8	349181.8
18	292.5	18	67.5	90.0	1302.6	884.6	157.5	2	2.72	3.2				11702.2	19820.4	22877	23021.2
19	292.5	27	67.5	90.0	1302.6	884.6	157.5	1.9	2.26	2.8				3599.4	8169.6	8503.6	10571.6
20	315	9	90.0	45.0	1302.6	884.6	157.5	2.5	3.2	3.7				157895	196382	191447	310131
21	315	18	90.0	45.0	1302.6	884.6	157.5	2.4	3	3.5				4482	6436	6413	9599
22	315	27	90.0	45.0	1302.6	884.6	157.5	2.3	2.8	3.2				1362	1911.2	1888	3025
23	292.5	9	90.0	67.5	1302.6	884.6	157.5	2.4	3	3.5				130837.8	167104	181879.4	277422.2
24	292.5	18	90.0	67.5	1302.6	884.6	157.5	2.2	2.8	3.4				3396	5026.4	5888.2	7779.4
25	292.5	27	90.0	67.5	1302.6	884.6	157.5	2.1	2.6	2.9				974.4	1337.12	1428	2143
26	270	9	90.0	90.0	1302.6	884.6	157.5	2.1	2.7	3.5	26.5	34.6	40.2	90252	123187	167528	228359
27	270	18	90.0	90.0	1302.6	884.6	157.5	2	2.6	3.2	20.5	29.1	31.9	1767	2912	5101	5050
28	270	27	90.0	90.0	1302.6	884.6	157.5	1.9	2.3	2.7	11.4	16.9	27.2	393	476	738	820

References

[1] L. Wang, F. Aslani, A review on material design, performance, and practical application of electrically conductive cementitious composites, Construct. Build. Mater. 229 (2019), 116892.
[2] P. Feng, et al., The significance of dispersion of nano-SiO2 on early age hydration of cement pastes, Mater. Des. 186 (2020), 108320, https://doi.org/10.1016/j.matdes.2019.108320.
[3] J.B. Sun, Mechanical, chemical and hydrothermal activation for waste glass reinforced cement, Construct. Build. Mater. (2021). https://doi.org/10.1016/j.conbuildmat.2021.124361.
[4] Wei Wa, et al., Generative design in building information modelling (BIM): Approaches and requirements, Sensors 21 (6) (2021), 5439, https://doi.org/10.3390/s21165439.
[5] W. Dong, et al., Piezoresistive properties of cement-based sensors: review and perspective, Construct. Build. Mater. 203 (2019) 146–163, https://doi.org/10.1016/j.conbuildmat.2019.01.081.
[6] D.G. Meehan, et al., Electrical-resistance-based sensing of impact damage in carbon fiber reinforced cement-based materials 21 (1) (2010) 83–105.
[7] B. Han, S. Ding, X. Yu, Intrinsic self-sensing concrete and structures: a review, Measurement 59 (2015) 110–128, https://doi.org/10.1016/j.measurement.2014.09.048.
[8] L. Chen, et al., Systematic study on mechanical and electronic properties of ternary VAlN, TiAlN and WAlN systems by first-principles calculations, Ceram. Int. 47 (6) (2021) 7511–7520, https://doi.org/10.1016/j.ceramint.2020.11.090.
[9] D. Wang, et al., Investigation on the Poor Fluidity of Electrically Conductive Cement-Graphite Paste: Experiment and Simulation, vol. 169, 2019, 107679.
[10] Farhad Aslani, et al., Mechanical behavior of fiber-reinforced self-compacting rubberized concrete exposed to elevated temperatures, J. Mater. Civ. Eng. 131 (12) (2019).
[11] J. Li, et al., Mechanical and conductive performance of electrically conductive cementitious composite using graphite, steel slag, and GGBS, Struct. Concr. (2020).
[12] P. Xie, et al., Determination of blast-furnace slag content in hardened concrete by electrical conductivity methods, Cem. Concr. Aggregates 17 (1) (1995) 79–83.
[13] L. Wang, F. Aslani, Electrical resistivity and piezoresistivity of cement mortar containing ground granulated blast furnace slag, Construct. Build. Mater. 263 (2020), 120243, https://doi.org/10.1016/j.conbuildmat.2020.120243.
[14] B. Lothenbach, K. Scrivener, R. Hooton, Supplementary cementitious materials, Cement Concr. Res. 41 (12) (2011) 1244–1256.
[15] J. Zhu, et al., Automatically processing IFC clipping representation for BIM and GIS integration at the process level, Appl. Sci. 10 (6) (2020) 2009.
[16] C. Qin, et al., DTCNNMI: a deep twin convolutional neural networks with multi-domain inputs for strongly noisy diesel engine misfire detection, Measurement 180 (2021), 109548, https://doi.org/10.1016/j.measurement.2021.109548.
[17] B. Han, X. Yu, J. Ou, Chapter 2 - compositions of self-sensing concrete, in: B. Han, X. Yu, J. Ou (Eds.), Self-Sensing Concrete in Smart Structures, Butterworth-Heinemann, 2014, pp. 13–43.
[18] W. Jiao, et al., Utilization of steel slags to produce thermal conductive asphalt concretes for snow melting pavements, J. Clean. Prod. (2020), 121197.
[19] Y. Ju, T. Shen, D. Wang, Bonding behavior between reactive powder concrete and normal strength concrete, Construct. Build. Mater. 242 (2020), 118024, https://doi.org/10.1016/j.conbuildmat.2020.118024.
[20] Z. Lei, et al., Study on solid waste pyrolysis coke catalyst for catalytic cracking of coal tar, Int. J. Hydrogen Energy 45 (38) (2020) 19280–19290, https://doi.org/10.1016/j.ijhydene.2020.05.075.
[21] P.S. Humbert, J. Castro-Gomes, CO2 activated steel slag-based materials: a review, J. Clean. Prod. 208 (2019) 448–457.
[22] Yunchao Tang, et al., Fracture behavior of a sustainable material: Recycled concrete with waste crumb rubber subjected to elevated temperatures, J. Clean. Prod. (2021) 66–74. https://doi.org/10.1016/j.jclepro.2021.128553.
[23] J. Zhang, et al., Sustainable utilization of bauxite residue (Red Mud) as a road material in pavements: a critical review, Construct. Build. Mater. (2020), 121419, https://doi.org/10.1016/j.conbuildmat.2020.121419.
[24] D. Xu, et al., Analytical approach for crack identification of glass fiber reinforced polymer–sea sand concrete composite structures based on strain dissipations, Struct. Health Monit. (2020), 1475921720974290, https://doi.org/10.1177/1475921720974290.
[25] Samuel, A.L.J.I.J.o.r. and development, 3, Some Studies in Machine Learning Using the Game of Checkers, vol. 3, 1959, pp. 210–229.
[26] N. Zhao, et al., One-step fabrication of biomass-derived hierarchically porous carbon/MnO nanosheets composites for symmetric hybrid supercapacitor, Appl. Surf. Sci. 526 (2020), 146696, https://doi.org/10.1016/j.apsusc.2020.146696.
[27] C. Liu, et al., Crossing thyristor branches based hybrid modular multilevel converters for DC line faults, IEEE Trans. Ind. Electron. (2020), https://doi.org/10.1109/TIE.2020.3026277.

[28] Junbo Sun, et al., Machine-Learning-Aided prediction of flexural strength and ASR expansion for waste glass cementitious composite, Appl. Sci. 11 (15) (2021). https://doi.org/10.3390/app11156686.
[29] V. Singh, N. Gu, X. Wang, A theoretical framework of a BIM-based multi-disciplinary collaboration platform, Autom. ConStruct. 20 (2) (2011) 134–144.
[30] Y. Liu, et al., Wear and heat shock resistance of Ni-WC coating on mould copper plate fabricated by laser, Journal of materials research and technology 9 (4) (2020) 8283–8288, https://doi.org/10.1016/j.jmrt.2020.05.083.
[32] J. Sun, et al., Machine learning-aided design and prediction of cementitious composites containing graphite and slag powder, Journal of Building Engineering (2021), 102544.
[33] J. Sun, et al., Prediction of permeability and unconfined compressive strength of pervious concrete using evolved support vector regression, Construct. Build. Mater. 207 (2019) 440–449, https://doi.org/10.1016/j.conbuildmat.2019.02.117.
[34] B. Mou, Y. Bai, Experimental investigation on shear behavior of steel beam-to-CFST column connections with irregular panel zone, Eng. Struct. 168 (2018) 487–504, https://doi.org/10.1016/j.engstruct.2018.04.029.
[35] C.J. Burges, A tutorial on support vector machines for pattern recognition, Data Min. Knowl. Discov. 2 (2) (1998) 121–167.
[36] H. Li, et al., Multi-objective optimization of PEM fuel cell by coupled significant variables recognition, surrogate models and a multi-objective genetic algorithm, Energy Convers. Manag. 236 (2021), 114063, https://doi.org/10.1016/j.enconman.2021.114063.
[37] H. Salehi, R. Burgueño, Emerging artificial intelligence methods in structural engineering, Eng. Struct. 171 (2018) 170–189, https://doi.org/10.1016/j.engstruct.2018.05.084.
[38] J.-S. Chou, C.-F. Tsai, Concrete compressive strength analysis using a combined classification and regression technique, Autom. ConStruct. 24 (2012) 52–60.
[39] Y. Sun, et al., Determination of Young's modulus of jet grouted coalcretes using an intelligent model, Eng. Geol. 252 (2019) 43–53.
[40] K. Duan, S.S. Keerthi, A.N. Poo, Evaluation of simple performance measures for tuning SVM hyperparameters, Neurocomputing 51 (2003) 41–59.
[41] J. Sun, et al., The effect of graphite and slag on electrical and mechanical properties of electrically conductive cementitious composites, Construct. Build. Mater. 281 (2021), 122606.
[42] J.-S. Chou, N.-T. Ngo, A.-D. Pham, Shear strength prediction in reinforced concrete deep beams using nature-inspired metaheuristic support vector regression, J. Comput. Civ. Eng. 30 (1) (2016), 04015002.
[43] Y. Yu, et al., Expansion prediction of alkali aggregate reactivity-affected concrete structures using a hybrid soft computing method, Neural Comput. Appl. 31 (12) (2019) 8641–8660.
[44] X. Jiang, S. Li, BAS: Beetle Antennae Search Algorithm for Optimization Problems, arXiv preprint arXiv:1710.10724, 2017.
[45] Y. Yang, et al., Flexible carbon-fiber/semimetal Bi nanosheet arrays as separable and recyclable plasmonic photocatalysts and photoelectrocatalysts, ACS Appl. Mater. Interfaces 12 (22) (2020) 24845–24854, https://doi.org/10.1021/acsami.0c05695.
[46] X.-S. Yang, Engineering Optimization: an Introduction with Metaheuristic Applications, John Wiley & Sons, 2010.
[47] J. Zhang, et al., Multi-objective Beetle Antennae Search Algorithm, 2020 arXiv preprint arXiv:2002.10090.
[48] Y. Sun, et al., Optimized neural network using beetle antennae search for predicting the unconfined compressive strength of jet grouting coalcretes, Int. J. Numer. Anal. Methods GeoMech. 43 (4) (2019) 801–813.
[49] J. Zhang, et al., Multi-objective optimization of concrete mixture proportions using machine learning and metaheuristic algorithms, Construct. Build. Mater. 253 (2020), 119208.
[50] R. Yao, et al., Preparation and characterization of novel glass–ceramic tile with microwave absorption properties from iron ore tailings 378 (2015) 367–375.
[51] C.J.B. Standard, China, GB/T, 50081-2002 Method for Testing Mechanical Properties of Normal Concrete, 2002.
[52] B. Kolani, et al., Hydration of slag-blended cements, Cement Concr. Compos. 34 (9) (2012) 1009–1018.
[53] D. Ionescu, T. Meadowcroft, P. Barr, Early-age hydration kinetics of steel slags, Adv. Cement Res. 13 (1) (2001) 21–30.
[54] F.J. Baeza, et al., Influence of Recycled Slag Aggregates on the Conductivity and Strain Sensing Capacity of Carbon Fiber Reinforced Cement Mortars, vol. 184, 2018, pp. 311–319.
[55] A. Smola, B. Schölkopf, A tutorial on support vector regression, Stat. Comput. 14 (3) (2004) 199–222, https://doi.org/10.1023/B:STCO.0000035301.49549.88.
[56] D. Basak, S. Pal, D.C. Patranabis, Support vector regression, Neural Information Processing-Letters and Reviews 11 (10) (2007) 203–224.
[57] S. Lahiri, K. Ghanta, The Support Vector Regression with the parameter tuning assisted by a differential evolution technique: study of the critical velocity of a slurry flow in a pipeline, Chem. Ind. Chem. Eng. Q. 14 (2008), https://doi.org/10.2298/CICEQ0803191L.
[58] S. Boyd, L. Vandenberghe, Convex Optimization, Cambridge University Press, 2004.
[59] J. Wang, H.J.a.p.a. Chen, BSAS: Beetle Swarm Antennae Search Algorithm for Optimization Problems, 2018.
[60] C.-W. Hsu, C.-C. Chang, C.-J. Lin, A Practical Guide to Support Vector Classification, 2003.
[61] A. Baykasoğlu, A. Öztaş, E. Özbay, Prediction and multi-objective optimization of high-strength concrete parameters via soft computing approaches, Expert Syst. Appl. 36 (3) (2009) 6145–6155.
[62] J. Hu, et al., Object traversing by monocular UAV in outdoor environment, Asian J. Contr. (2020), https://doi.org/10.1002/asjc.2415.
[63] J. Zhu, et al., Complexity analysis of prefabrication contractors' dynamic price competition in mega projects with different competition strategies, 2018, Complexity (2018).
[64] M. Klammer, et al., Pareto optimization identifies diverse set of phosphorylation signatures predicting response to treatment with dasatinib, PloS One 10 (6) (2015), e0128542, https://doi.org/10.1371/journal.pone.0128542.
[65] P. Cortez, M.J. Embrechts, Opening black box data mining models using sensitivity analysis, in: 2011 IEEE Symposium on Computational Intelligence and Data Mining (CIDM), IEEE, 2011.
[66] Z. Lei, et al., Study on denitration and sulfur removal performance of Mn–Ce supported fly ash catalyst, Chemosphere 270 (2021), 128646, https://doi.org/10.1016/j.chemosphere.2020.128646.
[67] P. Cortez, M.J. Embrechts, Using sensitivity analysis and visualization techniques to open black box data mining models, Inf. Sci. 225 (2013) 1–17, https://doi.org/10.1016/j.ins.2012.10.039.
[68] L. Wang, et al., Practical algorithm for stochastic optimal control problem about microbial fermentation in batch culture, Optimization Letters 13 (3) (2019) 527–541.
[69] K. Janković, et al., The influence of nano-silica and barite aggregate on properties of ultra high performance concrete, Construct. Build. Mater. 126 (2016) 147–156.
[70] M. Zhang, et al., Effects of graphite particles/Fe3+ on the properties of anoxic activated sludge, Chemosphere 253 (2020), 126638, https://doi.org/10.1016/j.chemosphere.2020.126638.
[71] X. Li, et al., Non-contact manipulation of nonmagnetic materials by using a uniform magnetic field: experiment and simulation, J. Magn. Magn Mater. 497 (2020), 165957, https://doi.org/10.1016/j.jmmm.2019.165957.
[72] E. Anastasiou, et al., Utilization of fine recycled aggregates in concrete with fly ash and steel slag 50 (2014) 154–161.
[73] Z. Hou, et al., Direct ink writing of materials for electronics-related applications: a mini review, Frontiers in Materials 8 (2021) 91, https://doi.org/10.3389/fmats.2021.647229.
[74] N. Gao, et al., Design, fabrication and sound absorption test of composite porous metamaterial with embedding I-plates into porous polyurethane sponge, Appl. Acoust. 175 (2021), 107845, https://doi.org/10.1016/j.apacoust.2020.107845.
[75] A.N. Givi, et al., Experimental investigation of the size effects of SiO2 nano-particles on the mechanical properties of binary blended concrete, Compos. B Eng. 41 (8) (2010) 673–677.
[76] C. Wu, et al., Ontological knowledge base for concrete bridge rehabilitation project management, Autom. ConStruct. 121 (2021), 103428.